Efficient kinetic Lattice Boltzmann simulation of three-dimensional magneto-hydrodynamic turbulence

Emmanuel Lévêque, Alessandro de Rosis, Fabio Feraco, Raffaele Marino

Efficient kinetic Lattice Boltzmann simulation of three-dimensional magneto-hydrodynamic turbulence

Emmanuel Lévêque[1]†, Alessandro de Rosis[2], Fabio Feraco[1,3] and Raffaele Marino[1]

[1]Laboratory of Fluid Mechanics and Acoustics, UMR CNRS 5509, Ecole Centrale de Lyon, Univ Lyon, F-69134 Ecully cedex, France

[2]Department of Mechanical, Aerospace and Civil Engineering, The University of Manchester, Manchester, M13 9PL, United Kingdom

[3]Dipartimento di Fisica, Università della Calabria, 87036 Rende, Italy

(Received xx; revised xx; accepted xx)

The opportunity of using a kinetic Lattice Boltzmann (LB) approach for the numerical simulation of three-dimensional magneto-hydrodynamic (MHD) turbulence is examined. A significant advantage of dealing with a kinetic representation of the plasma (even in simulating the MHD scales) is that the derivatives of the magnetic field are directly encompassed in the solution, thus allowing for an intrinsically accurate description of the small-scale current density structures. A novel LB framework is proposed here to address the three-dimensional Orszag-Tang vortex problem at increasing Reynolds numbers. Our analysis shows that both small-scale dynamics and spectral properties of LB runs are compatible with the outcome of analogous pseudo-spectral simulations (Mininni *et al.* 2006) generated with a well-established pseudo-spectral code (Mininni *et al.* 2011; Pouquet *et al.* 2019). This study shows how phenomenology of MHD turbulence is suitably captured by our LB simulations, which reproduced it with accuracy and computational efficiency. The newly developed algorithm couples two LB schemes for fluid dynamics including the Lorentz force and the magnetic induction equation respectively. The fluid incompressibility is achieved in the low-Mach-number limit, whereas the divergence-free condition for the magnetic field is preserved within machine precision. It is also emphasized how such novel scheme is amenable to a high level of parallelism and can exploit the computational power of many-core accelerators such as Graphic Processing Units (GPUs) thus leading to very advantageous turnaround times. This is supported by a preliminary benchmark that shows the high scalability of our model implementation.

1. Introduction

Magnetohydrodynamics (MHD) is used to describe the motion of quasi-neutral fluid material elements containing at least two types of particles with opposite charges such as in liquid metals, electrolytes, hot ionized gases in the presence of a magnetic field or rarefied plasma such as the solar wind (Marino *et al.* 2008) at scales where the local thermal equilibrium is granted. MHD brings together the concepts of fluid dynamics and electromagnetism and is used to describe plasma dynamics in the frame of the space weather and the heliospheric physics (Marino *et al.* 2012), nuclear fusion, industrial processing of liquid metals, etc. It provides also the theoretical framework for the development of a wide spectrum of technological devices ranging from magnetohydrodynamic

† Email address for correspondence: emmanuel.leveque@ec-lyon.fr

pump to magnetic drug targeting inside the human body and plasma thrusters to adjust the orbits of the satellites (Désangles *et al.* 2020).

Numerical simulations represent a major tool of investigation of MHD flows in situations where experiments cannot be accomplished because it is too dangerous or not feasible due to technical constraints. When the flow is turbulent, pseudo-spectral methods are widely recognized as one of the best options, as they allow for an accurate representation of all the scales involved in turbulent motions (Patterson & Orszag 1971). In the present work, a novel lattice Boltzmann (LB) implementation is proposed as an alternative to classical pseudo-spectral codes in order to reach a profitable trade-off between accuracy of the simulated plasma dynamics and computational efficiency. Unlike more conventional methods that solve the dynamics of neutral and magnetized flows at the macroscopic level, the LB method operates at the kinetic (or mesoscopic) level.Therefore, the flow complexity emerges from the repetition of simple rules of collision and streaming of collections of particles living on a regular lattice (Krüger *et al.* 2016). Originally validated by the intuition, the link between such idealized description and the Boltzmann equation is now well established, thus placing the method on solid theoretical and mathematical grounds (Shan & He 1998). Furthermore, the method is computationally very efficient due to its particulate nature and its focus on the local dynamics (Körner *et al.* 2006).

A decisive contribution to the kinetic simulation of MHD flows has been made by Dellar (2002) who demonstrated that the LB framework could be extended to encompass both the fluid dynamics driven by the Lorentz force and the magnetic induction equation. The LB scheme introduced by Dellar fully complies with the MHD equations (in a weakly-compressible formulation, see §2) but is prone to numerical instabilities. These latter are mainly related to the growing of spurious non-hydrodynamic high-order modes when strong velocity gradients develop in the flow (Latt & Chopard 2006). To overcome such limitation, De Rosis *et al.* (2018) successfully proposed to replace the classical Bhatnagar-Gross-Krook (BGK) collision operator (Bhatnagar *et al.* 1954*a*) by a collision in the space of central moments allowing an explicit damping of non-hydrodynamic statistical moments. This recent progresses have encouraged us to deepen into the LB modelling and evaluate its practical utility for the study of MHD turbulence.

The paper is organized as follows. In §2, the kinetic scheme is detailed and its numerical implementation discussed. The three-dimensional Orszag-Tang vortex problem at increasing Reynolds numbers is then used as a reference test case of MHD turbulent flows in §3. It is shown how characteristic features of MHD turbulence are suitably captured by our developed kinetic scheme; comparisons are carried out with the pseudo-spectral MHD turbulence realization by Mininni *et al.* (2006). In §4, the computational efficiency of the scheme is presented, tested and discussed through a preliminary benchmark associated with the porting of the algorithm on some leading-edge devices. Finally, conclusions and potential applications are discussed in the context of plasma studies in the last section. With this work, we want to demonstrate that LB has reached maturity to address complex MHD flows, opening a new horizon for its application in the research on plasma flows.

2. Methodology

In this section, we shall first recall the macroscopic dynamics that are simulated. The related underlying kinetic schemes are detailed in a second step.

2.1. *The macroscopic governing equations*

At the macroscopic level, the MHD description for an electrically conductive fluid consists of the incompressible Navier-Stokes equations including the Lorentz force, *i.e.*

$$\partial_t \boldsymbol{u} + (\boldsymbol{u}\cdot\boldsymbol{\nabla})\,\boldsymbol{u} = -\frac{1}{\rho_0}\boldsymbol{\nabla} p + \frac{1}{\rho_0}\boldsymbol{J}\times\boldsymbol{B} + \nu\Delta\boldsymbol{u} \tag{2.1}$$

$$\boldsymbol{\nabla}\cdot\boldsymbol{u} = 0 \tag{2.2}$$

where ρ_0 and ν denote the mass density and kinematic viscosity, respectively. These equations are coupled with the Maxwell-Faraday equation for the magnetic field

$$\partial_t \boldsymbol{B} = -\boldsymbol{\nabla}\times\boldsymbol{E} = -\boldsymbol{\nabla}\times\left(-\left(\boldsymbol{u}\times\boldsymbol{B}\right) + \eta\boldsymbol{\nabla}\times\boldsymbol{B}\right) \tag{2.3}$$

under the divergence-free constraint

$$\boldsymbol{\nabla}\cdot\boldsymbol{B} = 0. \tag{2.4}$$

In Eq. (2.3), the electric field $\boldsymbol{E}$ is usually approximated according to the resistive Ohm's law by $\boldsymbol{E} = -\left(\boldsymbol{u}\times\boldsymbol{B}\right) + \eta\boldsymbol{\nabla}\times\boldsymbol{B}$, where η is the (constant) magnetic resistivity of the fluid. In Eq. (2.1), the electric current density expresses as $\boldsymbol{J} = \frac{1}{\mu_0}\boldsymbol{\nabla}\times\boldsymbol{B}$. However, the magnetic permittivity μ_0 can be absorbed in the magnetic field (by replacing $\boldsymbol{B}$ by $\mu_0^{1/2}\boldsymbol{B}$) so that the Lorentz force $\boldsymbol{J}\times\boldsymbol{B}$ eventually simplifies as $(\boldsymbol{\nabla}\times\boldsymbol{B})\times\boldsymbol{B}$. Note that this change of variables does not affect the other equations.

In a kinetic approach, the condition of incompressibility cannot be strictly fulfilled (particles cannot move at an infinite speed) but only approached in a *low-Mach limit* (McNamara & Zanetti 1988). This latter is achieved when the speed of sound waves (c_s) becomes much larger that the macroscopic fluid velocity or, equivalently, when the Mach number $\mathrm{Ma} = |\boldsymbol{u}|/c_s \to 0$. Therefore, the original incompressible Eqs. (2.1) and (2.2) should be abandoned in favour of a compressible formulation

$$\partial_t\left(\rho\boldsymbol{u}\right) + \boldsymbol{\nabla}\cdot\left(\rho\boldsymbol{u}\otimes\boldsymbol{u} + p\boldsymbol{I} + \frac{1}{2}|\boldsymbol{B}|^2\boldsymbol{I} - \boldsymbol{B}\otimes\boldsymbol{B}\right) = \rho\nu\Delta\boldsymbol{u} \tag{2.5}$$

$$\partial_t\rho + \boldsymbol{\nabla}\cdot\left(\rho\boldsymbol{u}\right) = 0 \tag{2.6}$$

in which the Lorentz force has been expressed in a conservative manner as minus the divergence of the Maxwell stress tensor $M_{\alpha\beta} = \frac{1}{2}|\boldsymbol{B}|^2\delta_{\alpha\beta} - B_\alpha B_\beta$. By convention, the tensor product $(\boldsymbol{a}\otimes\boldsymbol{b})_{\alpha\beta} = a_\alpha b_\beta$. Compressibility imposes to resort to an additional *equation of state* between the pressure, the mass density and the temperature of the fluid. Here, the low-Mach limit justifies to use the simple isothermal relation†

$$p = \rho c_s^2 \tag{2.7}$$

where c_s identifies as the speed of sound (Krüger *et al.* 2016). For the magnetic field, the simulated equation is unchanged and writes in a divergence form (resembling Eq. (2.5)) as

$$\partial_t\boldsymbol{B} + \boldsymbol{\nabla}\cdot\left(\boldsymbol{u}\otimes\boldsymbol{B} - \boldsymbol{B}\otimes\boldsymbol{u}\right) = \eta\boldsymbol{\Delta}\boldsymbol{B}. \tag{2.8}$$

The divergence-free condition on the magnetic field is preserved by Eq. (2.8) which means that it is sufficient to impose $\boldsymbol{\nabla}\cdot\boldsymbol{B} = 0$ initially. A particular attention will be paid to verify that this condition is indeed well preserved numerically.

The coupled system of Lattice Boltzmann schemes introduced in the following is designed to conform to Eq. (2.5), Eq. (2.6), Eq. (2.7) and Eq. (2.8) at the macroscopic level.

† Relative fluctuations of temperature and mass density are both $O(\mathrm{Ma}^2)$.

2.2. *Kinetic representation of the macroscopic governing equations*

Capturing the evolution of collections of fluid particles distributed throughout a regular lattice is here preferred to solving non-linear PDEs. It may sound unrealistic, however, the kinetic theory suggests that most of the details at this mesoscopic level play actually no role on macroscopic dynamics. Therefore, much simpler dynamics can be conceived by retaining in the kinetic framework only the basic features pertaining the macroscopic level. This is the rationale behind the LB method, which can be viewed as a minimalist and computationally efficient kinetic model. Such framework can be extended to simulate the dynamics of the magnetic field.

In the LB approach to classical hydrodynamics, macroscopic variables such as the fluid density or the velocity are given by the statistical moments

$$\rho(\boldsymbol{x},t)=\sum_{i=0}^{N-1} f_i(\boldsymbol{x},t) \quad \text{and} \quad \rho\boldsymbol{u}(\boldsymbol{x},t)=\sum_{i=0}^{N-1} f_i(\boldsymbol{x},t)\boldsymbol{c}_i \tag{2.9}$$

where the distribution functions $f_0, \ \cdots, \ f_{N-1}$ are associated with a discrete set of prescribed microscopic velocities $\boldsymbol{c}_0, \ \cdots, \ \boldsymbol{c}_{N-1}$. The sums replace here the integrals over $\boldsymbol{c}$ in the standard kinetic theory. In brief, this discretization stems from expanding (and truncating) the solution of the continuum Boltzmann equation onto a finite basis of Hermite polynomials in velocity, and resorting to a Gaussian quadrature formula to express statistical moments†. Therefore, the $f_i(\boldsymbol{x},t)$ evolve according a discrete-velocity analogue of the Boltzmann equation

$$\partial_t f_i+\boldsymbol{c}_i\cdot\boldsymbol{\nabla} f_i=-\frac{1}{\tau}\left(f_i-f_i^{(0)}(\rho,\boldsymbol{u})\right) \tag{2.10}$$

where the BGK approximation (Bhatnagar *et al.* 1954*b*) to the collision (right-hand side) term is often used. In this latter, the distribution functions $f_i(\boldsymbol{x},t)$ relax locally towards their values at absolute equilibrium with a unique relaxation time $\tau=\nu/c_s^2$ related to collisions. This is sufficient to ensure that the slowly varying (on timescales smaller than τ) solution of the hierarchy of statistical equations obtained from Eq. (2.10) satisfy the isothermal Navier-Stokes equations with third-order corrections in the Mach number. Eq. (2.10) is discretized in space and time by integration along characteristics to yield the LB scheme. The set of velocities $\boldsymbol{c}_0, \ \cdots, \ \boldsymbol{c}_{N-1}$ determines the lattice so that collections of particles move from one node to a neighbouring node during exactly one time step, then collide, reorient and spread again during the next time step, and so on. The LB scheme governs the evolution in time of the number of particles moving along each link of the lattice.

In the same way, the magnetic field can be represented as

$$\boldsymbol{B}(\boldsymbol{x},t)=\sum_{i=0}^{M-1}\boldsymbol{g}_i(\boldsymbol{x},t) \tag{2.11}$$

where the vector-valued distributions $\boldsymbol{g}_i(\boldsymbol{x},t)$ are associated with fractions of the magnetic field carried by particles evolving on a lattice superimposed on the fluid lattice. Interestingly, Dellar showed that it was possible to consider for the magnetic field a sub-lattice of the lattice used for the fluid.

† The discrete set of velocities may be thought of as the nodes in the Gaussian quadrature formula.

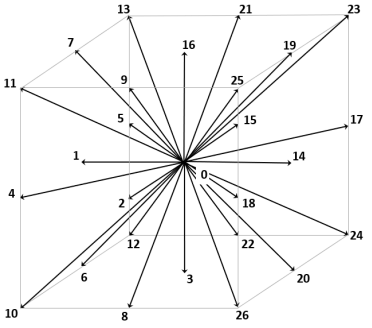

FIGURE 1. Set of microscopic velocities of the D3Q27 lattice. At each lattice node, microscopic velocities point towards the center, the 6 centers of faces, the 12 centers of edges and the 8 corners of a cube.

2.2.1. *Central-moment-based Lattice Boltzmann algorithm for the fluid*

For the fluid, the discretization (in velocity) of phase space refers here to a D3Q27 cubic lattice associated with the set of microscopic velocities $\{\boldsymbol{c}_i\}_{i=0,\ldots,26}$ given by the Cartesian components

$$
\begin{aligned}
|c_x\rangle &= [0,-1,0,0,-1,-1,-1,-1,0,0,-1,-1,-1,-1,1,0,0,1,1,1,1,0,0,1,1,1,1]^\top \\
|c_y\rangle &= [0,0,-1,0,-1,1,0,0,-1,-1,-1,-1,1,1,0,1,0,1,-1,0,0,1,1,1,1,-1,-1]^\top \\
|c_z\rangle &= [0,0,0,-1,0,0,-1,1,-1,1,-1,1,-1,1,0,0,1,0,0,1,-1,1,-1,1,-1,1,-1]^\top
\end{aligned}
$$

in lattice units (see Fig. 1). Lattice units are obtained by rescaling space and time by the lattice spacing and the time step of the LB algorithm, respectively. Note that the peculiar ordering of the $\boldsymbol{c}_i$ is consistent with the proposal made by Latt (2007) to swap and update distributions during the streaming step to halve the memory usage.

The lattice node values are the sets of distributions $|\mathrm{f}\rangle = [\mathrm{f}_0 \ldots \mathrm{f}_{26}]^\top$ associated locally with the particles moving along the links $i = 0, \ldots, 26$ with velocities $\boldsymbol{c}_0, \ldots, \boldsymbol{c}_{26}$. The LB scheme (in lattice units) advances the solution according to

$$
\mathrm{f}_i(\boldsymbol{x}+\boldsymbol{c}_i, t+1) = \mathrm{f}_i(\boldsymbol{x},t) - \omega\left[\mathrm{f}_i(\boldsymbol{x},t) - \mathrm{f}_i^{(0)}(\rho(\boldsymbol{x},t),\boldsymbol{u}(\boldsymbol{x},t))\right] \tag{2.12}
$$

which obviously resembles Eq. (2.10). Nevertheless, this resemblance is misleading because f_i does not exactly refers to the solution f_i of the discrete-velocity Boltzmann equation (Eq. (2.10)) but to

$$
\mathrm{f}_i = f_i + \frac{1}{2}\frac{\Delta t}{\tau}(f_i - f_i^{(0)}). \tag{2.13}
$$

This change of variable results from the use of a second-order accurate trapezoidal rule to approximate the integral of the collision term. It also calls for a redefinition of the relaxation time from τ to $\tau + \Delta t/2$ so that

$$
\frac{1}{\omega} = \left(\frac{\nu}{c_s^2 \Delta t} + \frac{1}{2}\right) \tag{2.14}
$$

where c_s refers to the sound speed. $\Delta x/\Delta t = \sqrt{3}c_s$ by construction so that $c_s = 1/\sqrt{3}$ in lattice units. On the hand, the formulation of the mass density and fluid velocity in

terms of statistical moments remains valid, *i.e.*

$$\rho(\boldsymbol{x},t)=\sum_{i=0}^{N-1}\mathrm{f}_i(\boldsymbol{x},t)\quad\text{and}\quad\rho\boldsymbol{u}(\boldsymbol{x},t)=\sum_{i=0}^{N-1}\mathrm{f}_i(\boldsymbol{x},t)\boldsymbol{c}_i \tag{2.15}$$

which justifies to some extent the qualification of f_i as a distribution function. Finally, Eq. (2.12) is commonly divided into a two-step *stream-collide* algorithm, in which a streaming step

$$\mathrm{f}_i(\boldsymbol{x}+\boldsymbol{c}_i,t+1)=\mathrm{f}_i^{\star}(\boldsymbol{x},t) \tag{2.16}$$

is consecutive to a local collision operation

$$\mathrm{f}_i^{\star}(\boldsymbol{x},t)=\mathrm{f}_i(\boldsymbol{x},t)+\omega\left[\mathrm{f}_i^{(0)}(\boldsymbol{x},t)-\mathrm{f}_i(\boldsymbol{x},t)\right]. \tag{2.17}$$

The superscript $\star$ denotes post-collision variables here and henceforth.

In classical fluids, the distribution $\mathrm{f}_i^{(0)}$ at equilibrium is given by the truncated Hermite expansion of the (continuous) Maxwell-Boltzmann equilibrium distribution. This expansion is commonly truncated at the second order, however, several groups (Malaspinas 2015; Coreixas *et al.* 2017, 2019; De Rosis & Luo 2019; De Rosis *et al.* 2019) have very recently shown that a gain in accuracy and stability was expected by accounting for higher-order terms. Here, the use of the D3Q27 lattice allows us to develop an equilibrium distribution up to the sixth-order:

$$\begin{aligned}
\mathrm{f}_i^{(0)}=w_i\rho\Bigg\{&1+\frac{\boldsymbol{c}_i\cdot\boldsymbol{u}}{c_s^2}+\frac{1}{2c_s^4}\Bigg[\mathcal{H}^{(2)}_{ixx}u_x^2+\mathcal{H}^{(2)}_{iyy}u_y^2+\mathcal{H}^{(2)}_{izz}u_z^2\\
&+2\Big(\mathcal{H}^{(2)}_{ixy}u_xu_y+\mathcal{H}^{(2)}_{ixz}u_xu_z+\mathcal{H}^{(2)}_{iyz}u_yu_z\Big)\Bigg]\\
&+\frac{1}{2c_s^6}\Bigg[\mathcal{H}^{(3)}_{ixxy}u_x^2u_y+\mathcal{H}^{(3)}_{ixxz}u_x^2u_z+\mathcal{H}^{(3)}_{ixyy}u_xu_y^2+\mathcal{H}^{(3)}_{ixzz}u_xu_z^2\\
&+\mathcal{H}^{(3)}_{iyzz}u_yu_z^2+\mathcal{H}^{(3)}_{iyyz}u_y^2u_z+2\mathcal{H}^{(3)}_{ixyz}u_xu_yu_z\Bigg]\\
&+\frac{1}{4c_s^8}\Bigg[\mathcal{H}^{(4)}_{ixxyy}u_x^2u_y^2+\mathcal{H}^{(4)}_{ixxzz}u_x^2u_z^2+\mathcal{H}^{(4)}_{iyyzz}u_y^2u_z^2\\
&+2\Big(\mathcal{H}^{(4)}_{ixyzz}u_xu_yu_z^2+\mathcal{H}^{(4)}_{ixyyz}u_xu_y^2u_z+\mathcal{H}^{(4)}_{ixxyz}u_x^2u_yu_z\Big)\Bigg]\\
&+\frac{1}{4c_s^{10}}\Bigg[\mathcal{H}^{(5)}_{ixxyzz}u_x^2u_yu_z^2+\mathcal{H}^{(5)}_{ixxyyz}u_x^2u_y^2u_z+\mathcal{H}^{(5)}_{ixyyzz}u_xu_y^2u_z^2\Bigg]\\
&+\frac{1}{8c_s^{12}}\mathcal{H}^{(6)}_{ixxyyzz}u_x^2u_y^2u_z^2\Bigg\}.
\end{aligned} \tag{2.18}$$

The weights w_i are related to the lattice connectivity with $w_{\mathrm{center}}=8/27$, $w_{\mathrm{face}}=2/27$, $w_{\mathrm{edge}}=1/54$ and $w_{\mathrm{corner}}=1/216$ (see Fig. 1). $\mathcal{H}_{\mathbf{i}}^{(\mathbf{n})}$ refers to the nth-order Hermite polynomial tensors in velocity $\boldsymbol{c}_i$. Eq. (2.18) reduces to the standard second-order truncated equilibrium distribution if $\mathcal{H}_{\mathbf{i}}^{(\mathbf{3})}$, $\mathcal{H}_{\mathbf{i}}^{(\mathbf{4})}$, $\mathcal{H}_{\mathbf{i}}^{(\mathbf{5})}$ and $\mathcal{H}_{\mathbf{i}}^{(\mathbf{6})}$ are neglected.

Although the BGK scheme is generally considered as the orthodox approach, it suffers from stability issues in the zero-viscosity limit or for non-vanishing Mach numbers unless the lattice spacing is dramatically reduced. This problem has been mainly addressed by modifying either the numerical discretization of Eq. (2.10) or the collision operator. If the former approach leads to more stable schemes, numerical accuracy is also considerably

degraded compared to the original LB stream-and-collide algorithm. This drawback has recently motivated many efforts in developing collision operators with improved stability, as recently reviewed by Coreixas *et al.* (2019).

Moment-based LB schemes rely on an isomorphism between the local set of particle distributions and a related basis of velocity moments. Hence, the main idea is to relax statistical moments rather than distributions with timescales that can be chosen to artificially damp spurious non-hydrodynamic moments while ensuring the correct relaxation of physical moments, *e.g.* density, velocity or momentum flux. In this way, stability can be considerably improved. However, since fluid dynamics is inherently non-linear, irreducible coupling artefacts appear in the hydrodynamics essentially in the form of an enhanced bulk viscosity (Coreixas *et al.* 2019). More recently, Geier showed that further improvement could be reached by considering statistical moments in the reference frame of the moving fluid rather than in the rest frame (Geier *et al.* 2006). This procedure allows us to reduce the insufficient degree of Galilean invariance of previous formulations, and to decrease the coupling artefacts between spurious and physical moments (Geier *et al.* 2007). Statistical moments computed in the moving frame are commonly called *central moments* (CMs). CMs-based LB schemes therefore promise to be an effective approach to simulate fluid flows in the regime of high Reynolds numbers.

A key ingredient of CMs schemes is the shift of particle velocities by the local fluid velocity, thus defining a new set of local microscopic velocities $\bar{\boldsymbol{c}}_i = \boldsymbol{c}_i - \boldsymbol{u}$ against which CMs are evaluated. In the present work, we consider the set of CMs

$$|\mathrm{k}\rangle = [\mathrm{k}_0 \dots \mathrm{k}_{26}]^\top = \mathrm{T}^\top |\mathrm{f}\rangle \quad \text{or} \quad \mathrm{k}_i = \langle \mathrm{T}_i | \mathrm{f} \rangle \quad \text{for each component} \tag{2.19}$$

where the (invertible) transformation matrix T is defined explicitly by the column vectors

$$\begin{aligned}
&|\mathrm{T}_0\rangle = |1\rangle \\
&|\mathrm{T}_1\rangle; |\bar{\mathrm{T}}_2\rangle; |\bar{\mathrm{T}}_3\rangle = [\bar{c}_{ix}]^\top; [\bar{c}_{iy}]^\top; [\bar{c}_{iz}]^\top \\
&|\mathrm{T}_4\rangle; |\mathrm{T}_5\rangle; |\mathrm{T}_6\rangle = [\bar{c}_{ix}\bar{c}_{iy}]^\top; [\bar{c}_{ix}\bar{c}_{iz}]^\top; [\bar{c}_{iy}\bar{c}_{iz}]^\top \\
&|\mathrm{T}_7\rangle; |\mathrm{T}_8\rangle; |\mathrm{T}_9\rangle = [\bar{c}_{ix}^2 - \bar{c}_{iy}^2]^\top; [\bar{c}_{ix}^2 - \bar{c}_{iz}^2]^\top; [\bar{c}_{ix}^2 + \bar{c}_{iy}^2 + \bar{c}_{iz}^2]^\top \\
&|\mathrm{T}_{10}\rangle; |\mathrm{T}_{11}\rangle; |\mathrm{T}_{12}\rangle = [\bar{c}_{ix}\bar{c}_{iy}^2 + \bar{c}_{ix}\bar{c}_{iz}^2]^\top; [\bar{c}_{ix}^2\bar{c}_{iy} + \bar{c}_{iy}\bar{c}_{iz}^2]^\top; [\bar{c}_{ix}^2\bar{c}_{iy} + \bar{c}_{iy}^2\bar{c}_{iz}]^\top \\
&|\mathrm{T}_{13}\rangle; |\mathrm{T}_{14}\rangle; |\mathrm{T}_{15}\rangle = [\bar{c}_{ix}\bar{c}_{iy}^2 - \bar{c}_{ix}\bar{c}_{iz}^2]^\top; [\bar{c}_{ix}^2\bar{c}_{iy} - \bar{c}_{iy}\bar{c}_{iz}^2]^\top; [\bar{c}_{ix}^2\bar{c}_{iy} - \bar{c}_{iy}^2\bar{c}_{iz}]^\top \\
&|\mathrm{T}_{16}\rangle = [\bar{c}_{ix}\bar{c}_{iy}\bar{c}_{iz}]^\top \\
&|\mathrm{T}_{17}\rangle; |\mathrm{T}_{18}\rangle; |\mathrm{T}_{19}\rangle = [\bar{c}_{ix}^2\bar{c}_{iy}^2 + \bar{c}_{ix}^2\bar{c}_{iz}^2 + \bar{c}_{iy}^2\bar{c}_{iz}^2]^\top; [\bar{c}_{ix}^2\bar{c}_{iy}^2 + \bar{c}_{ix}^2\bar{c}_{iz}^2 - \bar{c}_{iy}^2\bar{c}_{iz}^2]^\top; [\bar{c}_{ix}^2\bar{c}_{iy}^2 - \bar{c}_{ix}^2\bar{c}_{iz}^2]^\top \\
&|\mathrm{T}_{20}\rangle; |\mathrm{T}_{21}; |\mathrm{T}_{22}\rangle = [\bar{c}_{ix}^2\bar{c}_{iy}\bar{c}_{iz}]^\top; [\bar{c}_{ix}\bar{c}_{iy}^2\bar{c}_{iz}]^\top; [\bar{c}_{ix}\bar{c}_{iy}\bar{c}_{iz}^2]^\top \\
&|\mathrm{T}_{23}\rangle; |\mathrm{T}_{24}; |\mathrm{T}_{25}\rangle = [\bar{c}_{ix}\bar{c}_{iy}^2\bar{c}_{iz}^2]^\top; [\bar{c}_{ix}^2\bar{c}_{iy}\bar{c}_{iz}^2]^\top; [\bar{c}_{ix}^2\bar{c}_{iy}^2\bar{c}_{iz}]^\top \\
&|\mathrm{T}_{26}\rangle = [\bar{c}_{ix}^2\bar{c}_{iy}^2\bar{c}_{iz}^2]^\top.
\end{aligned} \tag{2.20}$$

The set of CMs at equilibrium is obtained the same way by

$$|\mathrm{k}^{(0)}\rangle = \left[\mathrm{k}_0^{(0)} \dots \mathrm{k}_{26}^{(0)}\right]^\top = \mathrm{T}^\top |\mathrm{f}^{(0)}\rangle \quad \text{or} \quad \mathrm{k}_i^{(0)} = \langle \mathrm{T}_i | \mathrm{f}^{(0)} \rangle \quad \text{for each component.} \tag{2.21}$$

Consequently, the sixth-order Hermite expansion (2.18) simply gives

$$\mathrm{k}_0^{(0)} = \rho, \quad \mathrm{k}_9^{(0)} = 3\rho c_s^2, \quad \mathrm{k}_{17}^{(0)} = \rho c_s^2, \quad \mathrm{k}_{18}^{(0)} = \rho c_s^4, \quad \mathrm{k}_{26}^{(0)} = \rho c_s^6 \tag{2.22}$$

and $\mathrm{k}_{1\dots8}^{eq} = \mathrm{k}_{10\dots16}^{eq} = \mathrm{k}_{19\dots25}^{eq} = 0$. Interestingly, only five CMs at equilibrium are non-zero. Furthermore, their values are the same as those given by the continuous Maxwell-Boltzmann distributions and are Galilean invariant. Therefore, our basis takes full advantage of the D3Q27 discretization.

Moment-based collision generalizes Eq. (2.17) as

$$|\mathrm{k}^\star\rangle = |\mathrm{k}\rangle - \Lambda\left(|\mathrm{k}\rangle - |\mathrm{k}^{(0)}\rangle\right) \tag{2.23}$$

where the collision matrix Λ is now introduced. The BGK approximation is recovered by simply taking $\Lambda = \omega\, \boldsymbol{I}$. Here, the idea is to relax moments individually. Therefore, Λ remains diagonal but with specific relaxation rate for each moment. The matrix adopted here is

$$\Lambda = \mathrm{diag}[1,\ 1,\ 1,\ 1,\ \omega,\ \omega,\ \omega,\ \omega,\ \omega,\ 1, \ldots,\ 1] \tag{2.24}$$

which leads explicitly to

$$\begin{aligned}
\mathrm{k}_0^\star &= \mathrm{k}_0^{(0)} \\
\mathrm{k}_4^\star &= (1-\omega)\,\langle T_4|\mathrm{f}\rangle \\
\mathrm{k}_5^\star &= (1-\omega)\,\langle T_5|\mathrm{f}\rangle \\
\mathrm{k}_6^\star &= (1-\omega)\,\langle T_6|\mathrm{f}\rangle \\
\mathrm{k}_7^\star &= (1-\omega)\,\langle T_7|\mathrm{f}\rangle \\
\mathrm{k}_8^\star &= (1-\omega)\,\langle T_8|\mathrm{f}\rangle \\
\mathrm{k}_9^\star &= \mathrm{k}_9^{(0)} \\
\mathrm{k}_{17}^\star &= \mathrm{k}_{17}^{(0)} \\
\mathrm{k}_{18}^\star &= \mathrm{k}_{18}^{(0)} \\
\mathrm{k}_{26}^\star &= \mathrm{k}_{26}^{(0)}
\end{aligned} \tag{2.25}$$

and $k_{1\ldots3}^\star = k_{10\ldots16}^\star = k_{19\ldots25}^\star = 0$. This collision matrix Λ allows us to increase the numerical stability through the damping of acoustic waves $\left(\mathrm{k}_9^\star = \mathrm{k}_9^{(0)}\right)$ and the equilibration of high-order moments $\left(\mathrm{k}_{10\ldots25}^\star = \mathrm{k}_{10\ldots25}^{(0)}\right)$. Eventually, the post-collision distributions are readily computed prior the unmodified streaming step (2.16) by inverting the transformation matrix T so that

$$\mathrm{f}_i^\star = \langle \mathrm{T}_i^{-1}|\mathrm{k}^\star\rangle \tag{2.26}$$

where T_i^{-1} refers to the column vectors of the inverse of T.

The above-outlined procedure refers to classical hydrodynamics. In the case of MHD, the momentum flux should be complemented with the Maxwell tensor, which can be simply incorporated in the previous scheme by adding the corresponding contribution to the distributions at equilibrium

$$\mathrm{f}_i^{\,\mathrm{mhd}(0)} = \mathrm{f}_i^{(0)} + \frac{w_i}{2c_s^4}\left[|\boldsymbol{B}|^2|\boldsymbol{c}_i|^2 - (\boldsymbol{c}_i\cdot\boldsymbol{B})^2\right] \tag{2.27}$$

and considering the CMs at equilibrium

$$\mathrm{k}_i^{(0)} = \langle \mathrm{T}_i|\mathrm{f}^{\,\mathrm{mhd}(0)}\rangle. \tag{2.28}$$

2.3. *Vector-valued BGK lattice Boltzmann scheme for the magnetic field*

The magnetic field is represented at the kinetic level by $\boldsymbol{B}(\boldsymbol{x},t) = \sum_i \boldsymbol{g_i}(\boldsymbol{x},t)$ where the sum spans over a set of vector-valued distributions $\boldsymbol{g_0},\ldots,\boldsymbol{g_{M-1}}$ associated locally with the discrete set of microscopic velocities $\boldsymbol{\xi}_0,\ldots,\boldsymbol{\xi}_{M-1}$. The lattice used for the magnetic field a priori differs from the lattice used for the fluid dynamics. However, it is desirable so that the nodes of the two lattices coincide so that $\boldsymbol{u}$ and $\boldsymbol{B}$ can be readily accessible

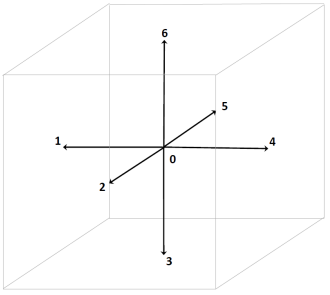

FIGURE 2. Set of microscopic velocities of the D3Q7 lattice. At each lattice node, microscopic velocities point towards the center, the 6 centers of faces of a cube.

by the two schemes without interpolation. Accordingly, Dellar established that a D3Q7 lattice (with much less symmetry than the D3Q27 lattice) was sufficient to comply with the induction equation (Dellar 2002). The corresponding discrete velocities (see Fig. 2) are

$$\begin{aligned} |\xi_x\rangle &= [0,-1,0,0,1,0,0]^\top \\ |\xi_y\rangle &= [0,0,-1,0,0,1,0]^\top \\ |\xi_z\rangle &= [0,0,0,-1,0,0,1]^\top \end{aligned} \tag{2.29}$$

in the same (Δx, Δt) lattice units as the fluid.

In the present case, the (vector-valued) distributions evolve according to

$$\mathbf{g}_i(+\boldsymbol{\xi}_i, t+1) = \mathbf{g}_i(\boldsymbol{x}, t) - \omega_m \left[\mathbf{g}_i(\boldsymbol{x}, t) - \mathbf{g}_i^{(0)}(\boldsymbol{x}, t)\right] \tag{2.30}$$

where the relaxation pulsation ω_m is now related to the magnetic resistivity by

$$\frac{1}{\omega_m} = \left(\frac{\eta}{C^2 \Delta t} + \frac{1}{2}\right) \tag{2.31}$$

with $\Delta x/\Delta t = 2C$ for the D3Q7 lattice. Here, C should be viewed as the speed at which a disturbance (of the magnetic field) is carried by "magnetic particles" between lattice nodes.

The distributions at equilibrium are expanded at first order as

$$\mathrm{g}_{i\alpha}^{(0)} = W_i \left[B_\alpha + \frac{1}{C^2}\xi_{i\beta}\left(u_\beta B_\alpha - B_\beta u_\alpha\right)\right] \tag{2.32}$$

where the weights $W_0 = 1/4$ and $W_{1\ldots6} = 1/8$. The D3Q7 lattice permits a substantial saving in storage, compensating partially for the need to apply the algorithm (2.30) to each component of $\mathbf{g}_i$. It is worth to emphasize that the dynamics of the magnetic field can be represented by using the simplest three-dimensional lattice that requires only seven velocities. This is due to the fact that $\boldsymbol{B}$ is evaluated as the zero-th order moment of $\boldsymbol{g}_i$, hence higher-order lattices (encompassing higher-order moments) are not required.

A key advantage of the kinetic approach is to directly yield macroscopic *fluxes* in terms of statistical moments of the distributions. Therefore, the viscous stress tensor is given by the second-order moment of the non-equilibrium part of the distributions for the fluid, so that the rate of strain expresses as

$$\mathrm{S}_{\alpha\beta} = -\frac{\omega}{2\rho c_s^2}\sum_i \left(\mathrm{f}_i - \mathrm{f}_i^{(0)}\right)\boldsymbol{c}_i \otimes \boldsymbol{c}_i \;+\; \mathrm{O}(\mathrm{Ma}^3) \tag{2.33}$$

where the $O(\mathrm{Ma}^3)$ term arises from the discretization in velocity of the phase space. In the same way, one can establish for the magnetic field (Pattison *et al.* 2008) that

$$\frac{\partial B_\alpha}{\partial x_\beta} = -\frac{\omega_m}{C^2}\sum_i \boldsymbol{\xi}_i \otimes \left(\mathbf{g}_i - \mathbf{g}_i^{(0)}\right) + O(\mathrm{Ma}^3) \tag{2.34}$$

from which the density of electric current readily reads (within a third-order correction in Mach) as

$$J_\gamma \equiv \epsilon_{\alpha\beta\gamma}\frac{\partial B_\alpha}{\partial x_\beta} = -\frac{\omega_m}{C^2}\sum_i \epsilon_{\alpha\beta\gamma}\left(\xi_{i\alpha} g_{i\beta} - 2\, u_\alpha B_\beta\right) \tag{2.35}$$

where $\epsilon_{\alpha\beta\gamma}$ is the alternating Levi-Civita tensor. Eq. (2.34) also provides a consistent approximation to the divergence of the magnetic field

$$\boldsymbol{\nabla}\cdot\boldsymbol{B} \simeq -\frac{\omega_m}{C^2}\mathrm{Tr}\left(\sum_i \boldsymbol{\xi}_i \otimes \mathbf{g}_i\right) \tag{2.36}$$

by noticing that $\mathrm{Tr}\left(\sum_i \boldsymbol{\xi}_i \otimes \mathbf{g}_i^{(0)}\right) = 0$. Furthermore, one can establish that the $O(\mathrm{Ma}^3)$ correction in Eq. (2.34) cancels out by taking the trace. Therefore, the modelling error is pushed to an higher order, so that $\boldsymbol{\nabla}\cdot\boldsymbol{B} = 0$ can be approximated with high accuracy by the condition $\mathrm{Tr}\left(\sum_i \boldsymbol{\xi}_i \otimes \mathbf{g}_i\right) = 0$ at the mesoscopic level. In practice, this later condition is actually maintained to machine round-off error by the LB algorithm (2.30) in numerical simulations. Finally, we would like to emphasize that the former kinetic approach provides an intrinsically accurate representation of the derivatives of the magnetic field, *i.e.* without resorting to any additional derivation operation. This is definitively a strength of the LB approach in the context of turbulent MHD flows that develop fine-scale magnetic structures.

3. Results

Our scheme is validated against the Orszag-Tang (OT) vortex problem often considered as a prototypical flow for the study of MHD turbulence. Here we will use as a reference the numerical results obtained in (Mininni *et al.* 2006) from pseudo-spectral simulations of the incompressible MHD equations (Mininni *et al.* 2011; Pouquet *et al.* 2019).

The investigated OT flow develops in a cubic box of size $L = 2\pi$ m with periodic boundary conditions in the three dimensions. The evolution is deterministic from the initial condition

$$\begin{aligned}
\boldsymbol{u}(\boldsymbol{x},0) &= u_0\,[-2\sin(y),\quad 2\sin(x),\quad 0]\\
\boldsymbol{B}(\boldsymbol{x},0) &= b_0\,[-2\sin(2y)+\sin(z),\quad 2\sin(x)+\sin(z),\quad \sin(x)+\sin(y)]\\
\rho(\boldsymbol{x},0) &= \rho_0
\end{aligned} \tag{3.1}$$

with $u_0 = 0.01$ and $b_0 = 0.8\ u_0$ in lattice units. The initial mass density is set to unity: $\rho_0 = 1$. The Mach number $\mathrm{Ma} = u_0/c_s \approx 0.0173$ approaching the incompressible limit with $\delta\rho/\rho_0 = \mathrm{O}(\mathrm{Ma}^2)$.

Each dimension is discretized into N grid points. The lattice spacing is therefore $\Delta x = L/N$ (m) and the time step Δt is such that $u_0\ \Delta x/\Delta t = 1$ m/s corresponding to the reference velocity used in the pseudo-spectral simulations. The Reynolds number based on the initial velocity is defined as $\mathrm{Re} = u_0 N/\nu$ in lattice units. For a given resolution, the viscosity is thus adjusted to reach the expected Reynolds number. Finally, the magnetic

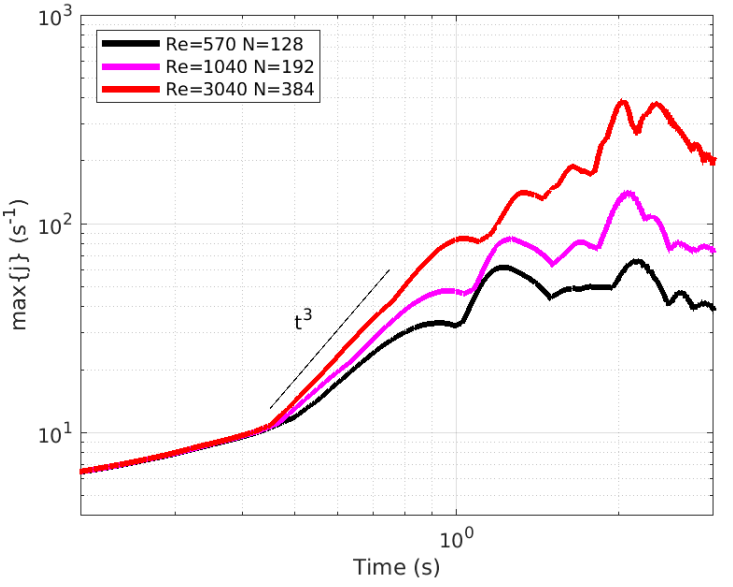

FIGURE 3. Time evolution of the maximum value (in the computational domain) of the electric current density at different Reynolds numbers.

Prandtl number is equal to unity so that $\eta = \nu$. We performed three LB simulations at Re = 570, 1040 and 3040 with respective resolutions 128^3, 256^3 and 384^3, comparable to the de-aliased pseudo-spectral simulations performed in (Mininni *et al.* 2006).

3.1. *Time evolution of the maximum of the electric current density*

The time evolution of the maximum value (in the computational domain) of the current density $J(\boldsymbol{x}, t)$ is plotted in Fig. 3. At early stages, $\max(J(\boldsymbol{x}, t))$ increases independently of the Reynolds number corresponding to the linear development of current and vorticity sheets. Then, a faster growth with a self-similar t^3 scaling develops before reaching a turbulent state in which complex current and vorticity sheet instabilities occur (see Fig. 4). The current density eventually decreases slowly under the effect of viscous and resistive dissipations. This behaviour fully agrees with the outcome of the pseudo-spectral simulations (see Mininni *et al.* 2006, Fig. 2).

3.2. *Fine-scale turbulent structures and spectral analysis*

The structures that generically develop in MHD turbulence are electric current sheets. Fig. 4 displays the volume of high current density in the simulation box at Re = 3040. Kelvin-Helmholtz instabilities (KHI) with rolling up of current sheets are visible, which is again compatible with what reported in (Mininni *et al.* 2006). This makes LB simulations of MHD flows suitable for the study of rarefied heliospheric and magnetospheric plasmas, where spacecraft observations have provided evidences of the presence of both KHI (Hasegawa *et al.* 2004) and fully developed MHD turbulence (Marino *et al.* 2008, 2011).

The rapid increase $\sim t^3$ of $\max(J)$ may be associated with energy populating abruptly a wide range of scales through strong non-linear interactions between dynamical modes. The kinetic and magnetic energy spectra are displayed in Fig. 5 for the simulation at Re=3040. As noticed from the evolution of the spectral energy at different times, both the the kinetic and the magnetic field are probably undergoing a direct turbulent

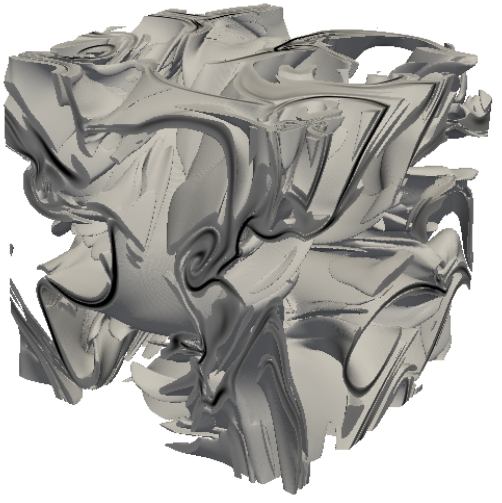

FIGURE 4. Regions of high current density obtained from a LB simulation at Re = 3040 with resolution 384^3. The snapshot is taken near the peak of the maximum value of $J(\boldsymbol{x}, t)$. Fine and elongated sheet structures resulting from stretching and rolling mechanisms are visible.

cascade. Turbulence appears to be fully developed when the simulation reaches the peak of the current density, this being suggested by the presence of a scaling range close to the characteristic Kolmorogov slope $k^{-5/3}$ at t=5, for nearly one decade of scales. The dynamical range of this simulation appears to be very good, with ~ 8 order of magnitude of separation in the power spectral density between the largest and the smallest resolved scale (see vertical axes in Fig. 5).

A final comment should be devoted to the divergence-free condition on the magnetic field. In our simulations, we checked that the equivalent kinetic condition $\mathrm{Tr}\left(\sum_i \boldsymbol{\xi}_i \otimes \mathbf{g}_i\right) = 0$ was maintained within 64-bit floating-point precision, *i.e.*

$$\max\left(|\boldsymbol{\nabla} \cdot \boldsymbol{B}|\right) \approx \max\left(\left|\mathrm{Tr}\left(\sum_i \boldsymbol{\xi}_i \otimes \mathbf{g}_i\right)\right|\right) = O(10^{-16}) \tag{3.2}$$

in lattice units. Let us recall that the reference value of the magnetic field is $b_0 = 8\,10^{-3}$ in lattice units. We also reconstructed the magnetic field in physical space and computed its divergence from a Fourier decomposition. At Re = 3040 with resolution 384^3, we obtained $\max(\boldsymbol{\nabla} \cdot \boldsymbol{B}) = O(10^0)$ in lattice units, which is considerably larger than the previous $O(10^{-16})$ estimate (given from the kinetic solution) but consistent with the second-order accuracy in space of the LB scheme. On the other hand, the average remains very low with $\langle \boldsymbol{\nabla} \cdot \boldsymbol{B} \rangle = O(10^{-14})$ in the reconstructed solution. Therefore, we may conclude that the adopted LB scheme complies (within machine round-off errors) with the divergence-free condition on the magnetic field, although this condition is not imposed in the design

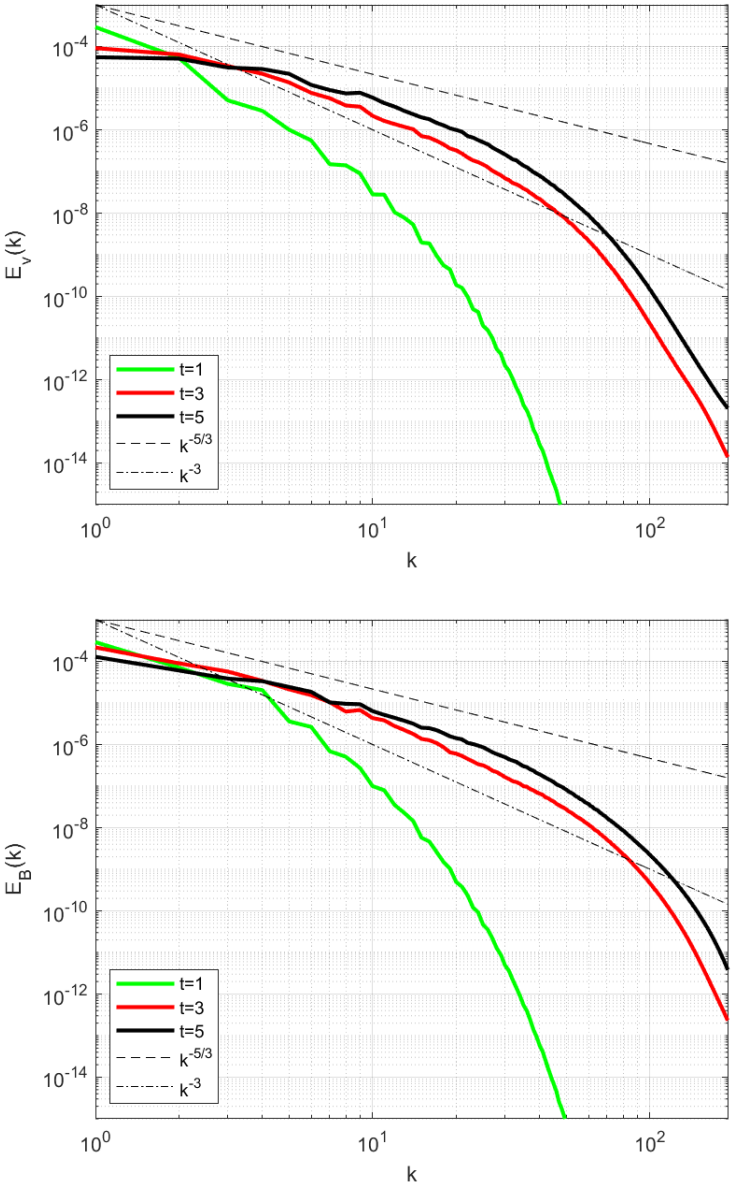

FIGURE 5. Kinetic and magnetic energy spectra in the linear regime ($t = 1$), in the self-similar regime ($t = 3$) and near the peak value of $\max(J)$ ($t = 5$) from the LB simulation at $\mathrm{Re} = 3040$. The scaling laws k^{-3} and $k^{-5/3}$ are given as reference. MHD turbulence eventually populates a wide range of wavenumbers k.

of the code, but only obtained as an approximation at second order in space in the reconstructed solution.

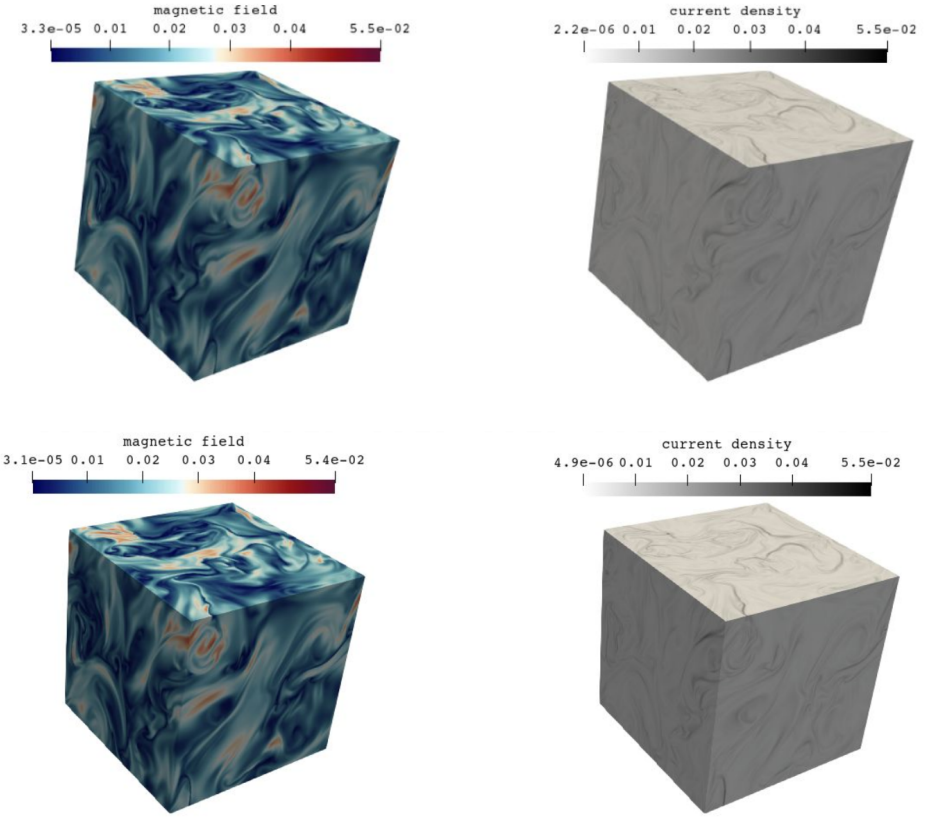

FIGURE 6. Snapshots of the Orszag-Tang solution at Re = 3040 with resolution 256^3 from a sequential run on CPU (top row) and a multi-threaded run accelerated by a NVIDIA Tesla V100-PCIE-16GB GPU (bottom row) after 15,000 iterations. The color bars indicate the maximum and the minimum of the magnitude in the snapshot.

4. Computational efficiency on various many-core devices

The intrinsic parallel nature of the LB algorithm makes it suitable to perform on many-core CPU (Central Processing Unit) and GPU (Graphic Processing Unit) high-performance-computing architectures. The computational efficiency of our kinetic LB three-dimensional MHD scheme is highlighted in the following through a preliminary benchmark based on Orszag-Tang vortex problem (with Re = 3040) ran at the resolution 256^3 on variety of multi-core systems. Each simulation performed 15000 time steps, needed to approximately reach the peak of current density. Multi-threading is handled automatically by using OpenCL – Open Computing Language, which allowed us to develop a *unique code* portable to the different targeted devices.

Briefly, the LB algorithm is data intensive and memory bound. In order to minimize the overhead due to uncoalesced memory accesses, a SoA (structure of array) data organization is preferred, *i.e* distribution functions with the same index of all lattice nodes are stored at consecutive memory addresses as an array, and then arrays of different distributions are stored one after the other. The collision and the streaming are combined in a unique computing kernel. Two distinct arrays are used to store the input and output distribution functions and swapped at the end of each time step, reaching an overall memory usage of 12.5 GB. In order to halve the memory usage, an *in-place* stream-

computing devices	wall-clock time Orszag-Tang problem at Re = 3040 256^3 – 15,000 iterations
1xCPU AMD Epyc 7302 (16 cores) @ 3GHz (128GB)	465 mins
2xCPU AMD Epyc 7502 (2x 32 cores) @ 2.5GHz (256GB)	41 mins
1xGPU NVIDIA GeForce RTX-2080-Super-8GB	50 mins (in-place)
1xGPU NVIDIA Tesla P100-PCIE-12GB	19,6 mins (in-place)
1xGPU NVIDIA Tesla P100-PCIE-16GB	8,2 mins
1xGPU NVIDIA Tesla V100-PCIE-16GB	5,75 mins

TABLE 1. Computational efficiency (in double precision) of the LB scheme on various many-core devices. The executable code was generated on each device with the same gcc compiling options: -std=c99 -O3 -march=native.

and-collide algorithm has also been tested (Latt 2007). This latter is detrimental to the performance but allowed us to use accelerators with limited memory. The performances are reported in Table 1. Let us mention these are only indicative and can certainly be optimized for each device, nevertheless, they provide a reliable overview of the remarkable computational efficiency of the LB scheme on multi-core devices, especially on high-end GPUs. The accuracy of the results is suitably maintained as evidenced by the comparison of the final snapshots in Fig. 6.

Finally, a multi-GPU implementation has also been developed to reach higher resolutions. The spatial domain is decomposed along a single direction and each GPU is assigned a sub-domain. There is a one-to-one mapping between the host CPU processes and the GPUs. Therefore, the exchange of boundary nodes between the GPUs is handled through memory transfers with the CPU processes and a message-passing interface (MPI) between these latter. As for the CPUs benchmark, the number of time steps corresponds approximately to the number of iterations needed to reach the peak of the current density. The multi-GPU performances are reported in Table 2 and indicate the good scalability of the LB algorithm. Again, it is worth to mention that a fine tuning of the code has not been conducted to optimize the performances; an improved speed-up should be achieved by overlapping computations, memory-copy operations and MPI communications for instance.

5. Conclusion

LB methods have reached sufficient maturity to be employed in the simulation of turbulent systems with many degrees of freedom, opening a new horizon for the numerical investigation of plasma flows. Stability issues, which has long been a handicap for the application of the LB schemes to turbulent flows, are now solved thanks to the use of improved collision operators without sacrificing accuracy. Furthermore, the computational efficiency of the LB schemes on many-core devices (in particular accelerators such as GPUs) allows for advantageous turn-around times.

As already mentioned, a significant advantage of dealing with a kinetic representation of the plasma is that the derivatives of the magnetic field are directly embedded in the solution, thus allowing for an intrinsically accurate description of the current density. This should for instance make it possible a step-forward in increasing the performance

cluster of GPUs	wall-clock time Orszag-Tang problem at Re = 3040 384^3 – 22,500 iterations
6x NVIDIA GeForce RTX-2080Ti-11GB	42 mins
8x NVIDIA GeForce RTX-2080Ti-11GB	33 mins
12x NVIDIA GeForce RTX-2080Ti-11GB	26 mins
	wall-clock time Orszag-Tang problem at Re = 5040 512^3 – 30,000 iterations
12x NVIDIA GeForce RTX-2080Ti-11GB	84 mins
16x NVIDIA GeForce RTX-2080Ti-11GB	67 mins

TABLE 2. Computational efficiency (in double precision) of the LB scheme on clusters of GPUs.

of Hall-MHD simulations, whose bottle-neck is represented by the need for a very small time-step in order to resolve the dynamics of the Hall terms. Furthermore, the kinetic LB approach allows us to add physical ingredients such as thermal effects, multi-species, etc. at the cost of new coupled lattice dynamics, therefore preserving the computational performance. In plasmas as well as in anisotropic fluids, turbulence has compete with waves in transferring energy across the scales (Marino *et al.* 2015*b*). The interplay of waves and turbulence is responsible for the emergence of new characteristic length scales and the existence of different regimes Marino *et al.* (2013); Feraco *et al.* (2018) in which various forms of energy can cascade to small or to large scales (Roche *et al.* (2009; Salort *et al.* 2012; Marino *et al.* 2014), or undergoing a dual energy cascade (Marino *et al.* 2015*a*). The computational efficiency of our LB model for the investigation of dynamics and energetics of anisotropic turbulent flows will allow us to run simulations of fluids and plasmas separating regimes (in terms of spatial and temporal scales) where different physical phenomena dominate. All that, together with the possibility to simulate flows in complex geometries and boundary conditions, provides our kinetic model with the potential to become a major tool of investigation of for magnetohydrodynamic plasmas in a variety of configurations of interest for engineering and scientific research.

We gratefully acknowledge the support of the Centre Blaise Pascal's IT test platform at ENS de Lyon for benchmarking our code on various many-core computing devices. Multi-GPU computations have been performed on the local HPC facilities (PSMN) at ENS de Lyon supported by the Auvergne-Rhône-Alpes region (GRANT CPRT07-13 CIRA) and the national Equip@Meso grant (ANR-10-EQPX-29-01). The test platform and the HPC center at ENS de Lyon operate the SIDUS solution (Quemener & Corvellec 2013) developed by Emmanuel Quemener.

REFERENCES

BHATNAGAR, P.L., GROSS, E.P. & KROOK, M. 1954*a* A model for collision processes in gases. I. small amplitude processes in charged and neutral one-component systems. *Phys. Rev.* **94** (3), 511.

Bhatnagar, P. L., Gross, E. P. & Krook, M. 1954*b* A model for collision processes in gases. i. small amplitude processes in charged and neutral one-component systems. *Phys. Rev.* **94**, 511–525.

Coreixas, Christophe, Chopard, Bastien & Latt, Jonas 2019 Comprehensive comparison of collision models in the lattice boltzmann framework: Theoretical investigations. *Phys. Rev. E* **100**, 033305.

Coreixas, Christophe, Wissocq, Gauthier, Puigt, Guillaume, Boussuge, Jean-François & Sagaut, Pierre 2017 Recursive regularization step for high-order lattice boltzmann methods. *Phys. Rev. E* **96** (3), 033306.

De Rosis, Alessandro, Huang, Rongzong & Coreixas, Christophe 2019 Universal formulation of central-moments-based lattice boltzmann method with external forcing for the simulation of multiphysics phenomena. *Physics of Fluids* **31** (11), 117102, arXiv: https://doi.org/10.1063/1.5124719.

De Rosis, Alessandro, Lévêque, Emmanuel & Chahine, Robert 2018 Advanced lattice boltzmann scheme for high-reynolds-number magneto-hydrodynamic flows. *J. Turbul.* **19** (6), 446–462.

De Rosis, Alessandro & Luo, Kai H. 2019 Role of higher-order hermite polynomials in the central-moments-based lattice boltzmann framework. *Phys. Rev. E* **99** (1), 013301.

Dellar, Paul J 2002 Lattice kinetic schemes for magnetohydrodynamics. *J. Comput. Phys.* **179** (1), 95–126.

Désangles, V, Shcherbanev, S, Charoy, T, Clément, N, Deltel, C, Richard, P, Vincent, S, Chabert, P & Bourdon, A 2020 Fast camera analysis of plasma instabilities in hall effect thrusters using a pod method under different operating regimes. *Atmosphere* **11**.

Feraco, F, Marino, R, Pumir, A, Primavera, L, Mininni, PD, Pouquet, A & Rosenberg, D 2018 Vertical drafts and mixing in stratified turbulence: sharp transition with froude number. *Europhys. Lett.* **123 (4)**, 44002.

Geier, M., Greiner, A. & Korvink, J.G. 2007 Properties of the cascaded lattice boltzmann automaton. *International Journal of Modern Physics C* **18** (4), 455–462, cited By 25.

Geier, Martin, Greiner, Andreas & Korvink, Jan G. 2006 Cascaded digital lattice boltzmann automata for high reynolds number flow. *Phys. Rev. E* **73**, 066705.

Hasegawa, H, Fujimoto, M, Phan, T-D, Rème, H, Balogh, A, Dunlop, MW, Hashimoto, C & TanDokoro, R 2004 Transport of solar wind into Earth's magnetosphere through rolled-up Kelvin-Helmholtz vortices. *Nature* **430**, 755–758.

Krüger, Timm, Kusumaatmaja, Halim, Kuzmin, Alexander, Shardt, Orest, Silva, Goncalo & Viggen, Erlend Magnus 2016 *The Lattice Boltzmann Method - Principles and Practice*.

Körner, Carolin, Pohl, Thomas, Rüde, Ulrich, Thürey, Nils & Zeiser, Thomas 2006 *Parallel Lattice Boltzmann Methods for CFD Applications*, , vol. 51, pp. 439–466.

Latt, Jonas 2007 Technical report: How to implement your ddqq dynamics with only q variables per node (instead of 2q). *Tufts University* pp. 1–8.

Latt, Jonas & Chopard, Bastien 2006 Lattice boltzmann method with regularized pre-collision distribution functions. *Math. Comput. Simulat.* **72** (2–6), 165 – 168.

Malaspinas, Orestis 2015 Increasing stability and accuracy of the lattice boltzmann scheme: recursivity and regularization. *arXiv preprint arXiv:1505.06900* .

Marino, R, Mininni, PD, Rosenberg, D & Pouquet, A 2013 Inverse cascades in rotating stratified turbulence: fast growth of large scales. *Europhys. Lett.* **102 (4)**, 4406.

Marino, R, Mininni, PD, Rosenberg, DL & Pouquet, A 2014 Large-scale anisotropy in stably stratified rotating flows. *Phys. Rev E* **90 (2)**, 023018.

Marino, R, Pouquet, A & Rosenberg, D 2015*a* Resolving the paradox of oceanic large-scale balance and small-scale mixing. *Phys. Rev. Lett.* **114 (11)**, 114504.

Marino, R, Rosenberg, D, Herbert, C & Pouquet, A 2015*b* Interplay of waves and eddies in rotating stratified turbulence and the link with kinetic-potential energy partition. *Europhys. Lett.* **112 (4)**, 49001.

Marino, R, Sorriso-Valvo, L, Carbone, V, Noullez, A, Bruno, R & Bavassano, B 2008 Heating the solar wind by a magnetohydrodynamic turbulent energy cascade. *Astrophys. J.* **677**, L71.

Marino, R, Sorriso-Valvo, L, Carbone, V, Veltri, P, Noullez, A & Bruno, R 2011 The magnetohydrodynamic turbulent cascade in the ecliptic solar wind: Study of Ulysses data. *Planetary and Space Sc.* **59**, 592–597.

Marino, R, Sorriso-Valvo, L, D'Amicis, R, Carbone, V, Bruno, R & Veltri, P 2012 On the occurence of the third-order scaling in high latitude Solar Wind. *Astrophys. J.* **750**, 41.

McNamara, Guy R. & Zanetti, Gianluigi 1988 Use of the boltzmann equation to simulate lattice-gas automata. *Phys. Rev. Lett.* **61**, 2332–2335.

Mininni, PD, Pouquet, AG & Montgomery, DC 2006 Small-scale structures in three-dimensional magnetohydrodynamic turbulence. *Phys. Rev. Lett.* **97** (24), 244503.

Mininni, PD, Rosenberg, D, Reddy, R & Pouquet, A 2011 A hybrid MPI-OpenMP scheme for scalable parallel pseudospectral computations for fluid turbulence. *Parallel Computing* **37**, 316–326.

Patterson, G. S. & Orszag, Steven A. 1971 Spectral calculations of isotropic turbulence: Efficient removal of aliasing interactions. *The Physics of Fluids* **14** (11), 2538–2541.

Pattison, MJ, Premnath, KN, Morley, NB & Abdou, MA 2008 Progress in lattice boltzmann methods for magnetohydrodynamic flows relevant to fusion applications. *Fusion Eng. Des.* **83** (4), 557–572.

Pouquet, A, Rosenberg, D, Stawarz, J & Marino, R 2019 Helicity dynamics, inverse, and bidirectional cascades in fluid and magnetohydrodynamic turbulence: A brief review. *Earth Space Sci.* **6**, 1–19.

Quemener, Emmanuel & Corvellec, Marianne 2013 Sidus—the solution for extreme deduplication of an operating system. *Linux J.* **2013** (235).

Roche, PE, Barenghi, CF & Lévêque, E (2009) Quantum turbulence at finite temperature: The two-fluids cascade. *Europhys. Lett.* **87 (5)**, 54006.

Salort, J, Chabaud, B, Lévêque, E & Roche, PE 2012 Energy cascade and the four-fifths law in superfluid turbulence. *Europhys. Lett.* **97 (3)**, 34006.

Shan, Xiaowen & He, Xiaoyi 1998 Discretization of the velocity space in the solution of the Boltzmann equation. *Phys. Rev. Lett.* **80**, 65–68.